General Disclaimer

One or more of the Following Statements may affect this Document

- This document has been reproduced from the best copy furnished by the organizational source. It is being released in the interest of making available as much information as possible.

- This document may contain data, which exceeds the sheet parameters. It was furnished in this condition by the organizational source and is the best copy available.

- This document may contain tone-on-tone or color graphs, charts and/or pictures, which have been reproduced in black and white.

- This document is paginated as submitted by the original source.

- Portions of this document are not fully legible due to the historical nature of some of the material. However, it is the best reproduction available from the original submission.

SC507.66AR

January 30, 1984

LUNAR SAMPLE ANALYSIS

ANNUAL REPORT NO. 12

For Period

January 1, 1983 through December 31, 1983

Contract No. NAS9-11539

Prepared for:

National Aeronautics and Space Administration
Lyndon B. Johnson Space Center
Science and Applications Directorate
Houston, Texas 77058

By:

R. M. Housley
Principal Investigator

This work was sponsored by the National Aeronautics and Space Administration.

Rockwell International
Science Center

Unclassified

SECURITY CLASSIFICATION OF THIS PAGE

REPORT DOCUMENTATION PAGE

1a. REPORT SECURITY CLASSIFICATION Unclassified	1b. RESTRICTIVE MARKINGS None
2a. SECURITY CLASSIFICATION AUTHORITY	3. DISTRIBUTION/AVAILABILITY OF REPORT Approved for public release; distribution unlimited.
2b. DECLASSIFICATION/DOWNGRADING SCHEDULE	
4. PERFORMING ORGANIZATION REPORT NUMBER(S) SC507.66AR	5. MONITORING ORGANIZATION REPORT NUMBER(S)
6a. NAME OF PERFORMING ORGANIZATION Rockwell International/ Science Center 6b. OFFICE SYMBOL (If applicable)	7a. NAME OF MONITORING ORGANIZATION
6c. ADDRESS (City, State and ZIP Code) P.O. Box 1085 Thousand Oaks, California 91360	7b. ADDRESS (City, State and ZIP Code)
8a. NAME OF FUNDING/SPONSORING ORGANIZATION NASA Lyndon B. Johnson Space Center 8b. OFFICE SYMBOL (If applicable)	9. PROCUREMENT INSTRUMENT IDENTIFICATION NUMBER NAS9-11539
8c. ADDRESS (City, State and ZIP Code) Science & Applications Directorate Houston, Texas 77058	10. SOURCE OF FUNDING NOS. PROGRAM ELEMENT NO. / PROJECT NO. / TASK NO. / WORK UNIT NO.
11. TITLE (Include Security Classification) LUNAR SAMPLE ANALYSIS	
12. PERSONAL AUTHOR(S) R. M. Housley, E. H. Cirlin, R. S. Rajan, E. R. Rambaldi, D. Want	
13a. TYPE OF REPORT Annual Report No. 12 13b. TIME COVERED FROM 01/01/83 TO 12/31/83	14. DATE OF REPORT (Yr., Mo., Day) January 27, 1984 15. PAGE COUNT 23
16. SUPPLEMENTARY NOTATION	
17. COSATI CODES FIELD / GROUP / SUB. GR.	18. SUBJECT TERMS (Continue on reverse if necessary and identify by block number) Enstatite, Qingzhen Meteorite, Unequilibrated, Chondrule, Matrix, Shock, Vigarano, ALHA 77003, Allende, Forsterite, Glass

19. ABSTRACT (Continue on reverse if necessary and identify by block number)

We present results from an extensive series of new high resolution scanning electron microscope studies of the very primative group of meteorites known as unequilibrated chondrites. These include quantitative analyses of micrometer sized phases and interpretation in terms of relevant phase equilibria. Several new meteorite minerals including high chromium metal, have been discovered.

20. DISTRIBUTION/AVAILABILITY OF ABSTRACT UNCLASSIFIED/UNLIMITED ☒ SAME AS RPT. ☐ DTIC USERS ☐	21. ABSTRACT SECURITY CLASSIFICATION Unclassified
22a. NAME OF RESPONSIBLE INDIVIDUAL R. M. Housley	22b. TELEPHONE NUMBER (Include Area Code) (805) 498-4545, X221 22c. OFFICE SYMBOL

DD FORM 1473, 83 APR EDITION OF 1 JAN 73 IS OBSOLETE.

Unclassified

SECURITY CLASSIFICATION OF THIS PAGE

Rockwell International
Science Center
SC507.66AR

SEM STUDIES OF WHITLOCKITE AND CHROMITE IN METAL-SULFIDE DROPLETS IN A C3 ALLAN HILLS METEORITE AND THEIR IMPLICATIONS. Eun-Hee Cirlin. Rockwell International Science Center, Thousand Oaks, CA 91360.

The meteorite ALHA 77003 is classified as type C3(1) and was referred to as type CO3(2). In this study whitlockite and chromite were found in metallic droplets in both chondrules and in matrix of polished section 77003,78 and were studied with a scanning electron microscope. Our SEM is equipped with a Princeton Gamma Tech x-ray analyzer, which is interfaced with a Kevex 7000 data analysis system. The quantitative analyses with standards using the program MAGIC V give better than 2% accuracy for major elements and satisfactory results for minor elements.

Recently Rambaldi et al (3) reported finding whitlockite in unequilibriated ordinary chondrites for the first time. They found the whitlockite in the interfaces between Si, Cr-rich kamacite and sulfides. In the present SEM studies, the whitlockite was found in all three phases, kamacite, taenite and troilite of metal-sulfide droplets in both chondrules and matrix. Many whitlockite worm-like grains were present along the edges of the metallic droplets (Fig. 1a). Troilite was present either as a shell around the metal (Fig. 1a), or with sharp crystal boundary lines (Fig. 1c). Also other small inclusions ($< 3\ \mu m$) of chromite and Fe-rich olivine were present in the metal (Fig. 1b and 1c). Table 1 shows analysis of typical whitlockite.

It was suggested for Apollo 14 samples that whitlockite was formed as a result of a reaction of schreibersite with surrounding pyroxene and oxygen (4). Our SEM studies showed that Ca in chondrule pyroxene, next to the whitlockite tooth in troilite is indeed depleted (Fig. 1d), suggesting that a similar reaction occurred in the meteorite. Since phosphorous has little solubility in sulfides (5), it must have been in the metal before the whitlockite grains were formed by oxidation. Then the metal was partially sulfurized some time later. Therefore, finding of similar whitlockite grains in both metal and troilite imply that the troilite formed from metal in a later stage after the whitlockite grains were formed and therefore after the chondrules were formed. Theoretical calculations by Olsen and Fuchs (6) supported by experimental work of Friel and Goldstein (7) can be used to show that in the solar nebular condensation process, the whitlockite would have formed at less than 680° K, whereas the troilite would be formed at around 700° K. This suggests that the troilite in ALHA 77003 was not formed during the solar nebular condensation sequence but was probably formed at a later time in a planetesimal (8).

The conclusion from the present study of this unequilibriated meteorite is that the troilite in chondrules resulted from sulfurization which occurred after the chondrules formed. This is in strong contrast to the conventional interpretation (9, page 179).

Table 1. Energy Dispersive X-ray Analysis of a Whitlockite

Element	Na	Mg	Si	P	Ca	Fe	Total
No. of cations in formula based on 8 oxygens	0.44	0.32	0.11	1.91	2.16	0.31	5.25

(1) Marvin U. B. and Mason B. (1982) Catalog of Meteorites from Victoria Land, Antarctica, 1978-1980, p. 85. (2) Swart P. K., Grady M. M., Norris S. J., Wright I. P. and Pillinger C. T. (1983) Lunar and Planetary Science XIV, p. 763. (3) Rambaldi E. R. and Rajan R. S. (1982) Meteoritics 17, p. 271. (4) El Goresy A., Taylor L. A. and Ramdohr P. (1972) Proc. Lunar Sci. Conf. 3rd, p. 333. (6) Olsen E. and Fuchs L. H. (1967) Icarus 6, p. 242. (5) Keil K. (1968) J. Geophys. Res., 73, p. 6945. (7) Friel J. J. and Goldstein J. I. (1976) Proc. Lunar Sci. Conf 7th, p. 791. (8) Armstrong J. T., Meeker G. P., Huneke J. C. and Wasserburg G. J. (1982) Geochimica et Cosmochimica Acta, 46, p. 575. (9) Dodd R. T. (1981) Meteor-

ites: A Petrologic-Chemical Synthesis, Cambridge University press.

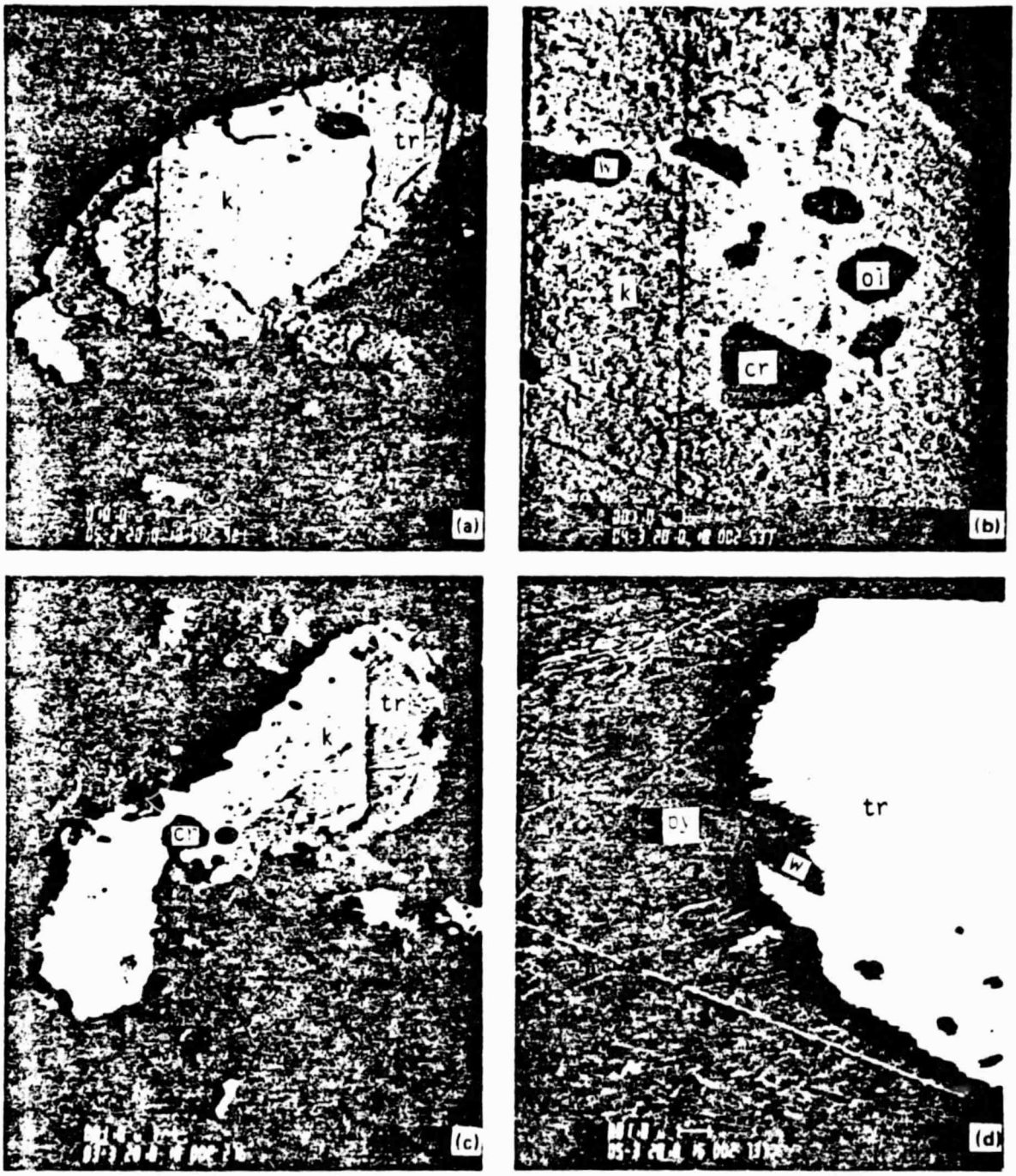

Fig. 1a. Backscattered electron image (BSE) of a metal droplet showing troilite shell around kamacite. Dark worm-like whitlockite grains are present in both kamacite and troilite along the edge of the droplet (b) BSE of small inclusions such as chromite and Fe-rich olivine present in kamacite (c) SEM photo of a metal droplet with chromite and whitlockite grains. Note a sharp boundary between kamacite and troilite (d) A whitlockite tooth in troilite. Ca in chondrule pyroxene near the whitlockite tooth is very depleted, suggesting that Ca from surrounding pyroxene reacted with phosphorous from the metal phase forming whitlockite.

OXIDIZED, REFRACTORY AND ALKALI-RICH COMPONENTS IN QINGZHEN ENSTATITE CHONDRITE: IMPLICATIONS ABOUT THEIR ORIGIN. E. R. Rambaldi, R. S.Rajan, Jet Propulsion Laboratory, California Institute of Technology, Pasadena, CA; R. M. Housley, Rockwell International Science Center, Thousand Oaks, CA; and D. Wang, Institute of Geochemistry, Academia Sinica, Guiyang, People's Republic of China.

Recent studies have shown that the highly unequilibrated enstatite chondrite Qingzhen contains a component that appears to have originated under relatively high oxidizing nebular conditions (1, 2). This component has been only incompletely reduced and consists of: a) relict grains of dusty olivine within incompletely melted chondrules (1), and b) enstatite grains, either isolated or in chondrule interiors (2). In order to improve our understanding of the origin of these materials, we are continuing our detailed chemical and textural studies of the silicate portion of Qingzhen. Some of the results are presented below.

Forsterite chondrules

Qingzhen contains a small population of chondrules which are enstatite-free and consist almost entirely of forsterite. Chondrule 3 consists of an intergrowth of forsterite crystals with minor amounts of Ca-pyroxene, plagioclase, metal and glass. The glass phase is small in size ($\leq$10 μm) and occurs both in interstitial regions and as inclusions within the olivine. Its composition varies from almost pure sodalitic ($\sim$ 7.5% Cl), to predominantly albitic, but other compositions having variable Ca and K contents have also been found. The Ca-pyroxene forms rims around the various glass phases and displays a wide compositional range (Al_2O_3 5.1-16.2; TiO_2 .2-1.3; CaO 15.5-22.9; MgO 13.4-23.5; Cr_2O_3 .6-1.6). A few grains of labradoritic plagioclase are associated with the glass and Ca-pyroxene. This is the first report of a Ca-rich plagioclase within an E-chondrite. The metal droplets have low Ni and Si and high Cr contents (Ni .03-2.3; Si .12-1.6; Cr .07-6.6). Their composition is suggestive of the reduction process of precursor oxidized material. The large compositional variation of the glass, metal and Ca-pyroxene phases indicates that, in spite of its igneous texture, chondrule 3 was never completely melted and homogenized. On a SiO_2-CaO+Al_2O_3-MgO ternary diagram, this chondrule falls into a region having a higher Mg/Si ratio than the enstatite-rich Qingzhen chondrules.

Ca, Al-rich chondrule

Chondrule 17 contains euhedral to subhedral enstatite crystals, representing about 1/5 of the chondrule volume, surrounded by a fine-grained intergrowth of labradoritic plagioclase (An 61-69) and SiO_2-rich glass. A few coarser grains of labradorite and Ca-pyroxene are scattered throughout the intergrowth. The whole chondrule is enriched in Ca (x10), Ti (x10), and Al (x5) relative to the enstatite-rich chondrules in Qingzhen.

In enstatite chondrites the bulk of the Ca and Ti occurs in sulfide phases (oldhamite and troilite) and only minor amounts of Ca are present in the interstitital glass of chondrules. This suggests that the precursor material of chondrule 17 originated in a less reducing, less sulfurizing and more refractory environment than that which existed at the formation location of the enstatite chondrites.

While minor amounts of forsterite have been reported within some chondrules of EH chondrites (3), our work on Qingzhen is the first report of the presence of forsteritic chondrules and chondrules containing large amounts of Ca, Al-silicates in this type of chondrite . The presence of these materials supports the dust-gas fractionation model suggested by Larimer and coworkers (4, 5) as a way to produce reducing conditions at the enstatite chondrite formation location. Thus, the refractory and oxidized components found in Qingzhen might represent materials which originated in dust-enriched nebular regions and were subsequently transported into an adjacent, more reducing environment, in which the Qingzhen chondrite was formed.

Albite-roedderite-metal assemblages

Qingzhen contains round metal-sulfide assemblages, some of which appear to have experienced reheating and, in some cases, melting. Small amounts of SiO_2 and enstatite often occur as inclusions within the metal of these assemblages. Within sulfide-poor assemblages we have observed substantial amounts of albite and roedderite included in the metal phase. In some cases the two phases are intimately intergrown and small amounts of SiO_2 are also present. Neither mineral has been found in other textural locations, with the exclusion of albitic glasses within chondrules.

As previously observed for Ca and Ti, in Qingzhen the bulk of the alkalis occur within major sulfide phases: djerfisherite (K), caswellsilverite (Na) and Cr-sulfides (Na, K) (6, 7). It is therefore surprising that alkali-bearing silicates are found in Qingzhen in this peculiar textural location. It appears that the metallic host has prevented the Na and K-silicates from being sulfurized by reaction with nebular H_2S, thus preserving their original compositional and textural characteristics. Even though the origin of these alkali-bearing assemblages is still unclear it is possible that they may also represent components originated in a different, more oxidizing nebular environment.

REFERENCES. 1) Rambaldi, E. R., et al. (1984) Earth Planet. Sci. Letters, in press. 2) Rambaldi, E. R., et al. (1984), Nature, submitted. 3) Binns, R. A. (1967) Am. Mineralogist, 52, p. 1549-1554. 4) Larimer, J. W. and Bartholomay, M. (1979) Geochim. Cosmochim. Acta, 43, p. 1455-1466. 5) Bartholomay, H. A. and Larimer, J. W. (1982) Meteoritics, 17, p. 180-181. 6) El Goresy, A. et al. (1983), Meteoritics, in press. 7) Rambaldi, E. R. et al. (1983) Meteoritics, in press.

CHARACTERISTICS OF REMELTED ALLENDE CHONDRULES AND MATRIX.

R. M. Housley and E. H. Cirlin. Rockwell International Science Center, Thousand Oaks, CA 91360.

As part of a more general observational and experimental investigation into the conditions under which various components in unequilibrated meteorites may have formed we have melted several Allende matrix samples and have remelted several Allende chondrules. This was done in the miniature graphite furnace of our atomic absorption apparatus (1), which provided conditions as reducing as plausible for any chondrule formation environment. Samples were rapidly heated to maximum temperatures in the range from 1350°C to 1750°C, held there for 2-3 seconds, and then cooled at 300-400°C per second.

The above procedure has the obvious shortcomings that sample compositions are not known in advance, and that the cooling rates are not controlled. Despite these, because of the very realistic nature of the starting materials, it provides important general information complimentary to that provided by previous more comprehensive and well controlled synthetic chondrule experiments starting with glass or oxide powders (2-4). It also provides information directly applicable to interpreting features seen in Allende chondrules.

The most important general feature observed in all our runs so far is that Na loss is almost complete while reduction of iron is fairly limited, even though the environment is highly reducing. Although kamacite is present in most samples, high FeO silicates and pentlandite always remain. This seems to rule out the possibility that chondrules could be produced by melting matrix in a reducing environment followed by the separation of reduced metal.

Except for containing large bubbles of doubtful significance, chondrules remelted at about 1500°C generally have textures typical of fresh porphyritic or microporphyritic chondrules as illustrated in Fig. 1a. A large fraction of the glass in actual Allende chondrules has been altered to secondary phases.

As expected with this thermal history, most of the forsteritic olivine in these remelted chondrules consists of relatively unchanged relic grains. As evidence of this the trapped melt inclusion shown in Fig. 2b is rich in Na and K, while these elements are undetectable in the nearby mesostasis glass. Little grain growth of olivine or crystallization of material from the glass is evident in the remelted chondrule illustrated in Figs. 1a and 1b.

In other cases several microns of olivine grain growth occurred, accompanied by the growth of micron sized crystals from the melt. This is illustrated in Figs. 1c and 1d. In general we believe the effect of remelting chondrules to this degree is largely to restore them to a conditions closely resembling their state before they were subjected to low temperature alteration.

In these remelted chondrules we never see magnetite, porous pentlandite, or Ca phosphate. These are all things we previously interpreted to be products of low temperature alteration (5). However, we do see virtually unchanged the healed cracks containing submicron chromite forcing us to consider the possibility that they formed at high temperature, probably by the oxidation of Cr^{++} which was in the olivine. The presence of 1 um sized chromite grains as shown in 1c and 1d, which are never seen in untreated Allende chondrules, indicates that Cr was not in the Cr^{+++} state when the chondrules formed.

REFERENCES

(1) Cirlin E. H. and Housley R. M. (1977) Proc. Lunar Sci. Conf. 8th, p. 3931-3940. (2) Blander M. and Katz J. L. (1967) Geochim. Cosmochim. Acta 31, p. 1025-1034. (3) Klein L. C., Fasano B. and Hewins R. H. (1980) Proc. Lunar Plant. Sci. Conf. 11th, p. 865-878. (4) Tsuchiyama A., Nagahara H. and Kushiro I. (1983) Proc. Conf. Chondrules and their Origins. (5) Housley R. M. and Cirlin E. H. (1983) Proc. Conf. Chondrules and their Origins.

Rockwell International
Science Center
SC507.66MR

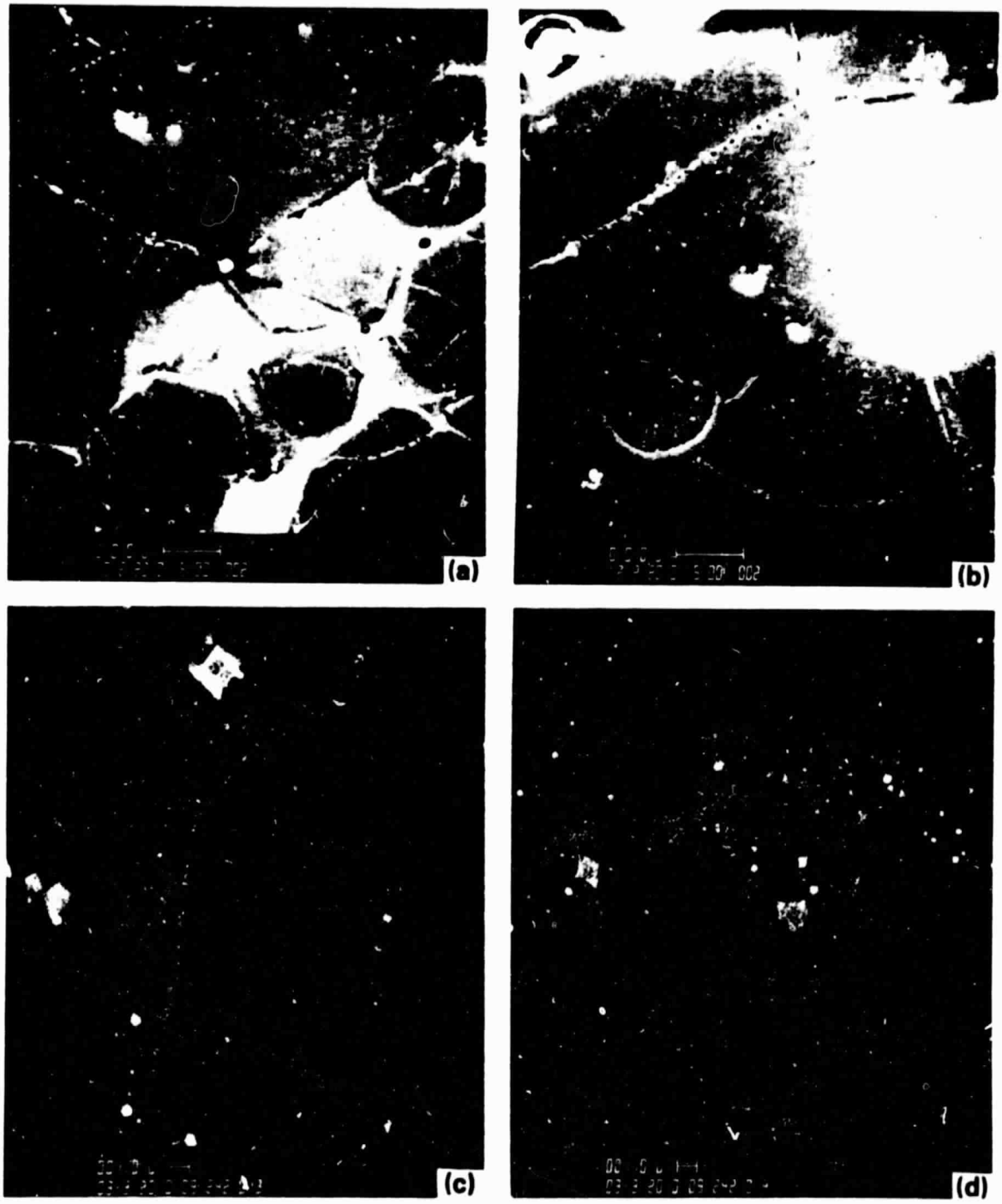

Fig. 1. Scanning electron micrographs of remelted chondrules. Microporphyritic texture in one remelted chondrule is illustrated in a and b along with submicron chromite along healed cracks. Grain growth of large olivines is illustrated by the backscattered electron images in c and d. About 1 micron of darker, more Mg-rich olivine surrounds the olivine cores on the right in c and on the bottom in d. This in turn is normally zoned to a very Fe-rich rim. Bright euhedral 1 um chromites are evident in the mesostases in c and d.

CHARACTERISTICS OF REMELTED ALLENDE CHONDRULES AND MATRIX.

R. M. Housley and E. H. Cirlin. Rockwell International Science Center, Thousand Oaks, CA 91360.

As part of a more general observational and experimental investigation into the conditions under which various components in unequilibrated meteorites may have formed we have melted several Allende matrix samples and have remelted several Allende chondrules. This was done in the miniature graphite furnace of our atomic absorption apparatus (1), which provided conditions as reducing as plausible for any chondrule formation environment. Samples were rapidly heated to maximum temperatures in the range from 1350°C to 1750°C, held there for 2-3 seconds, and then cooled at 300-400°C per second.

The above procedure has the obvious shortcomings that sample compositions are not known in advance, and that the cooling rates are not controlled. Despite these, because of the very realistic nature of the starting materials, it provides important general information complimentary to that provided by previous more comprehensive and well controlled synthetic chondrule experiments starting with glass or oxide powders (2-4). It also provides information directly applicable to interpreting features seen in Allende chondrules.

The most important general feature observed in all our runs so far is that Na loss is almost complete while reduction of iron is fairly limited, even though the environment is highly reducing. Although kamacite is present in most samples, high FeO silicates and pentlandite always remain. This seems to rule out the possibility that chondrules could be produced by melting matrix in a reducing environment followed by the separation of reduced metal.

Except for containing large bubbles of doubtful significance, chondrules remelted at about 1500°C generally have textures typical of fresh porphyritic or microporphyritic chondrules as illustrated in Fig. 1a. A large fraction of the glass in actual Allende chondrules has been altered to secondary phases.

As expected with this thermal history, most of the forsteritic olivine in these remelted chondrules consists of relatively unchanged relic grains. As evidence of this the trapped melt inclusion shown in Fig. 2b is rich in Na and K, while these elements are undetectable in the nearby mesostasis glass. Little grain growth of olivine or crystallization of material from the glass is evident in the remelted chondrule illustrated in Figs. 1a and 1b.

In other cases several microns of olivine grain growth occurred, accompanied by the growth of micron sized crystals from the melt. This is illustrated in Figs. 1c and 1d. In general we believe the effect of remelting chondrules to this degree is largely to restore them to a conditions closely resembling their state before they were subjected to low temperature alteration.

In these remelted chondrules we never see magnetite, porous pentlandite, or Ca phosphate. These are all things we previously interpreted to be products of low temperature alteration (5). However, we do see virtually unchanged the healed cracks containing submicron chromite forcing us to consider the possibility that they formed at high temperature, probably by the oxidation of Cr^{++} which was in the olivine. The presence of 1 um sized chromite grains as shown in 1c and 1d, which are never seen in untreated Allende chondrules, indicates that Cr was not in the Cr^{+++} state when the chondrules formed.

REFERENCES

(1) Cirlin E. H. and Housley R. M. (1977) Proc. Lunar Sci. Conf. 8th, p. 3931-3940. (2) Blander M. and Katz J. L. (1967) Geochim. Cosmochim. Acta 31, p. 1025-1034. (3) Klein L. C., Fasano B. and Hewins R. H. (1980) Proc. Lunar Plant. Sci. Conf. 11th, p. 865-878. (4) Tsuchiyama A., Nagahara H. and Kushiro I. (1983) Proc. Conf. Chondrules and their Origins. (5) Housley R. M. and Cirlin E. H. (1983) Proc. Conf. Chondrules and their Origins.

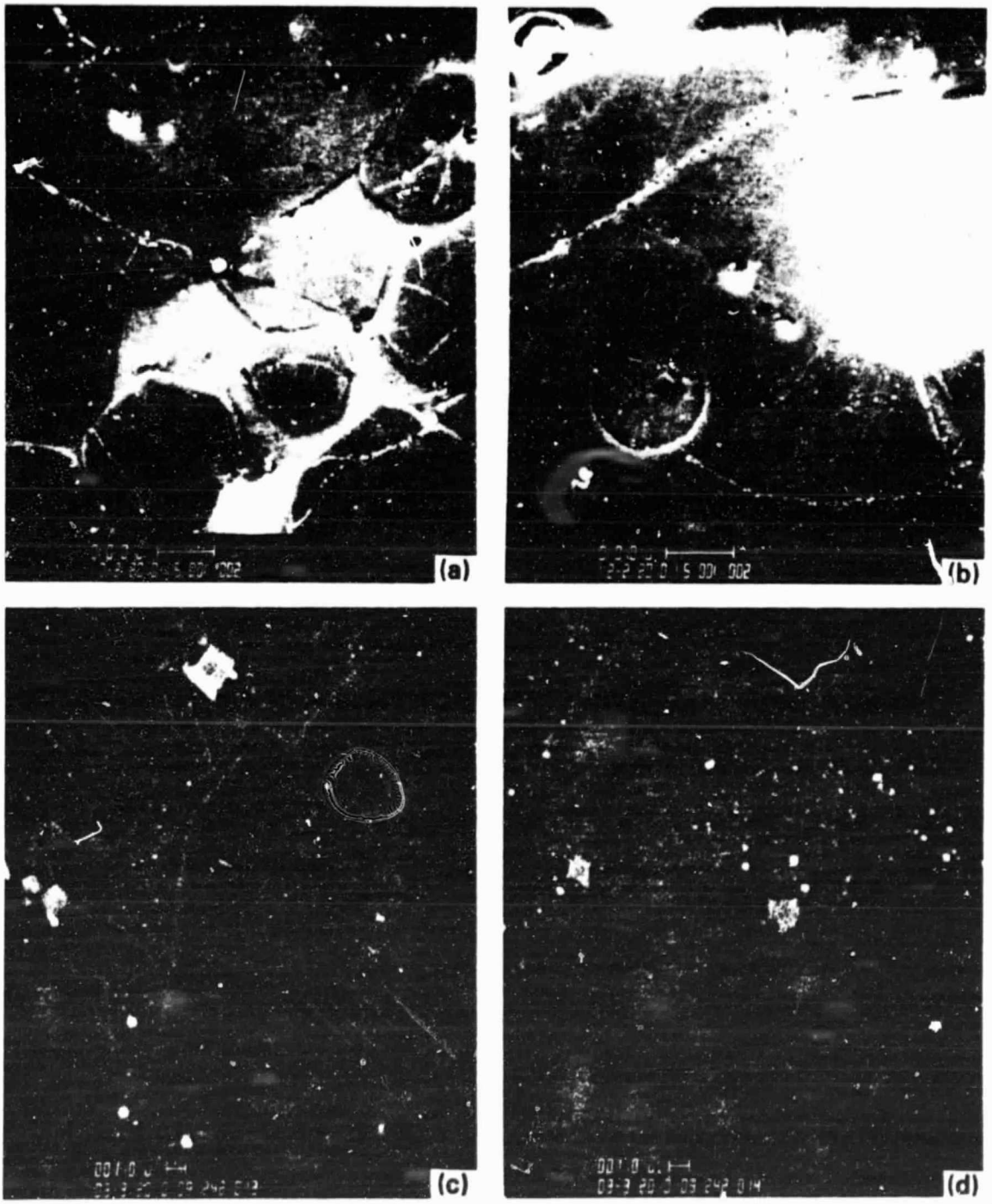

Fig. 1. Scanning electron micrographs of remelted chondrules. Microporphyritic texture in one remelted chondrule is illustrated in a and b along with submicron chromite along healed cracks. Grain growth of large olivines is illustrated by the backscattered electron images in c and d. About 1 micron of darker, more Mg-rich olivine surrounds the olivine cores on the right in c and on the bottom in d. This in turn is normally zoned to a very Fe-rich rim. Bright euhedral 1 um chromites are evident in the mesostases in c and d.

SCANNING ELECTRON MICROSCOPE STUDIES OF THE VIGARANO CV3 CHONDRITE: LARGE FORSTERITE GRAINS. R. M. Housley, Rockwell International Science Center, Thousand Oaks, CA 91360.

We are pursuing a comprehensive scanning electron microscope SEM study of the CV3 chondrite Vigarano. Our SEM is equipped with an energy dispersive x-ray detector which is interfaced with a Kevex 7000 data analysis system. We can obtain satisfactory major and minor element analyses using the program MAGIC V. All observations to date are on USNM section 477.

In general Vigarano is very complex with most large objects, such as chondrules, showing evidence of one or more episodes of severe shock. On the other hand the matrix contains delicate porous structures which could not have survived even mild shock. Therefore, as has been shown for Murchison (1), either the other components were shocked before being mixed with the present matrix, or the matrix is a secondary alteration product as is the case for Allende (2).

During our initial examination of several porphyritic chondrules in the section we noticed that some of the larger olivine grains were rounded or irregular in shape whereas most of the smaller ones were euhedral in outline. This led us to suspect that only partial melting occurred during the chondrule formation process and that these larger grains were relicts, even though they were not significantly different in composition from the smaller ones. In support of this interpretation we soon found nearly pure $MgAl_2O_4$ spinel crystals near the centers of two of these large olivine grains, although no spinel formed in the glassy mesostasis regions.

Our section contains eight irregular olivine fragments 600-1700 um in size which have similar composition ($Fa_{1.4}$-$Fa_{3.0}$) to the chondrule olivines which we believe to be relicts, and which are all larger than the largest euhedral chondrule olivine in the section. We are in the process of studying these grains in detail in the hope of attaining additional insight into the nature of chondrule precursor materials.

Although the Fa number varies some from place to place within these grains no well defined zoning trends have been discerned. Calcium ranges from <0.005 in two grains up to 0.019 atoms per atom of Si. Chromium was detected in six of the grains and ranges up to 0.007 atoms per atom Si in two of them. No correlations between Fe, Cr and Ca are apparent. Six spinel crystals were found in the grain shown in Fig. 1d. Four of these can be seen in 1e.

Although irregular in outline, five of these grains show a concentration of metal and sulfide droplets near their peripheries as illustrated in Figs. 1a and 1d. All of the grains show evidence of alteration and errosion near their borders as is illustrated in Fig. 1f, so the remaining grains may also once have had such enrichments. We tentatively interpret this peripheral metal enrichment to be the result of severe shock followed by annealing. Lobate glass inclusions as seen in Fig. 1d may also have been introduced in the same way. This may have been the chondrule forming event. Five of the grains as well as many olivines in chondrules also exhibit either parallel fractures or mosaic extinction or both as evidence of subsequent milder shocks.

Careful examination of these grains provides strong evidence that sulfide formation occurred after the metal was incorporated in them. The ratio of metal to sulfide always increases as the border is approached. Droplets in unfractured and unaltered olivine never contain sulfides. These must provide the best information about the precursor metal. They include droplets of Ni-rich taenite, droplets of kamacite with varying Ni contents and frequently significant Cr and P, and droplets containing both taenite and kamaeite. The olivine grains shown in Fig. 1a also contains a number of droplets consisting of kamacite plus Ni-rich schreibersite as shown in Fig. 1b. In addition, it

contains a unique metal grain containing about 60% Cr shown in Fig. 1c. Taken together these results seem to indicate that metal compositions were highly evolved at the time of incorporation, but that sulfide formation had not yet occurred.

(1) Lambert P. (1983) Lunar and Planetary Science XIV, p. 411-412.
(2) Housley R.M. and Cirlin E.H. (1983) Proc. Conf. Chondrules and their Origins.

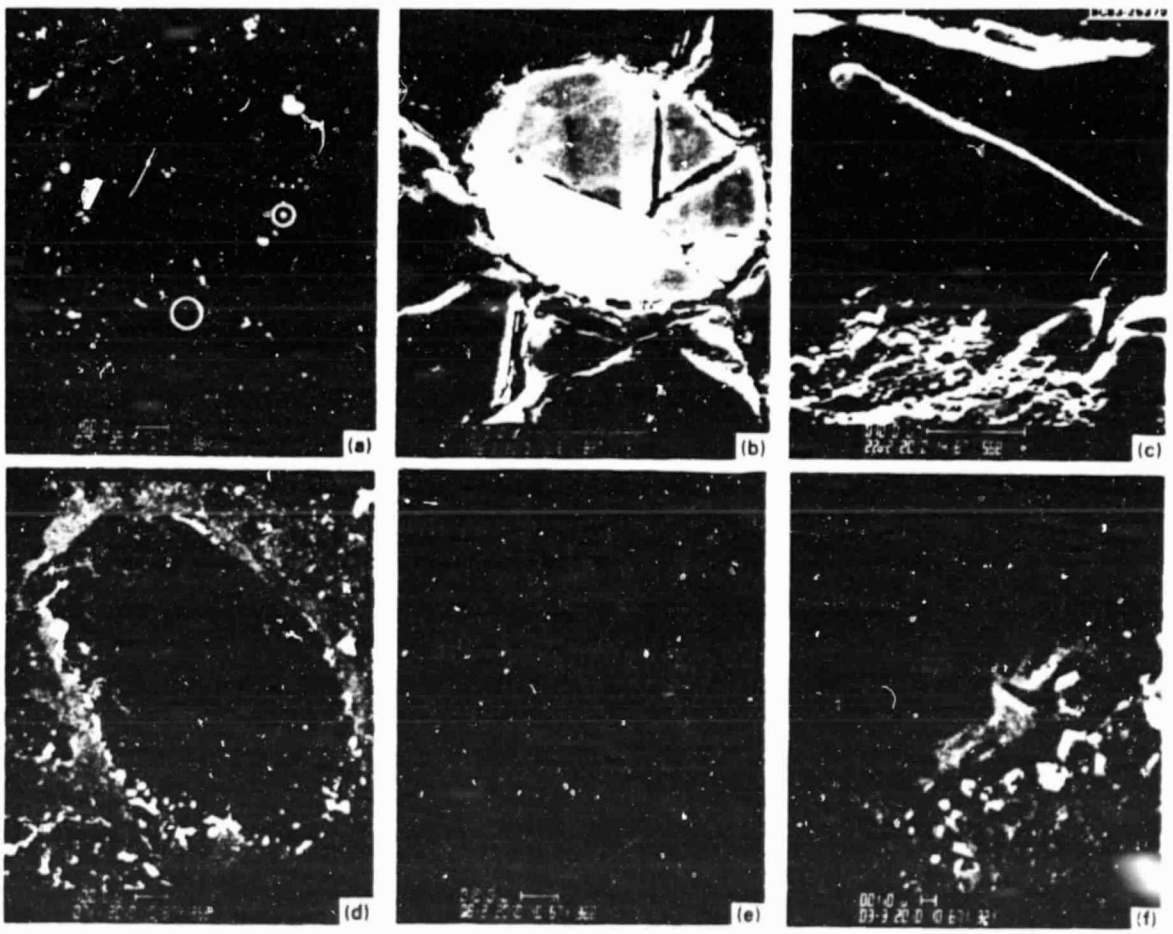

Fig. 1. Scanning electron micrographs of two large forsteritic olivine crystal fragments. Peripheral enrichment in metal and sulfides can be seen in the whole grain photos a and d. The droplet enclosed by the upper circle in a is kamacite. The long metal grain enclosed by the lower circle is enlarged in c. It contains 60% Cr. Marginal alteration along the lower border of a is illustrated in f. Diagonal light streaks are enriched in Cr and Fe. Area above long streak is forsterite. Dark area immediately below is enstatite which grades shortly in light Fe-rich silicate and then matrix. Three spinel grains from the crystal in d are shown near the center of e.

STATISTICAL FLAW DETECTION

APPLICATION TO FLAWS BELOW CURVED SURFACES

R.K.Elsley, K.W.Fertig, J.M.Richardson, R.S.Linebarger

Rockwell International Science Center
1049 Camino Dos Rios
Thousand Oaks, CA 91360

I. INTRODUCTION

The detection of the presence of flaws in structural materials is the most important function which Non-Destructive Evaluation (NDE) performs. As structures are designed to higher performance criteria and as safety and life cycle cost factors become more important, it becomes necessary to detect smaller and more difficult to find flaws. This paper presents a practical approach to the optimum detection of flaws in the presence of noise signals. A decision theoretic approach (described in more detail in a companion paper by Fertig, et al.[1]) is used to derive a detection algorithm which is adapted to the noise environment in which a particular measurement is being made. An automatic procedure for characterizing the noises and developing the optimum detection algorithm is presented. Two implementations of this approach have been tested on experimental data and show substantial improvement over conventional detection techniques. One is a flexible algorithm used for research purposes, and the other is a real-time algorithm suitable for field implementation.

This work was sponsored by the Center for Advanced Nondestructive Evaluation, operated by the Ames Laboratory, USDOE, for the Defense Advanced Research Projects Agency at the Air Force Wright Aeronautical Laboratories/Materials Laboratories under Contract No. W-7405-ENG-82 with Iowa State University.

II. THEORY

Ultrasonic measurements of small flaws are usually limited by the presence of one or a number of noise processes. The problem of flaw detection (or flaw characterization) is therefore one of distinguishing the flaw information from the accompanying noise information. The statistical approach to NDE involves taking specific account of the statistical nature of the noise processes when designing flaw detection or flaw characterization algorithms. The statistical approach has been used to develop a number of flaw characterization algorithms.[2-8] This paper describes the use of the same approach for flaw detection.

The first step in developing a statistical approach to flaw detection (or characterization) is to create a measurement model which describes both the signals due to the flaw and the signals due to noise sources. The second step is to calibrate the model by performing a set of measurements which determine the instrumental properties of the measurement system and the statistical properties of the noise mechanisms. The third step is to derive an algorithm which performs the detection (or characterization) in an optimal manner with respect to the signals and noises present.

The measurement model used in this paper is the following (expressed in the frequency domain):

$$M = XD_F A_F + XA_M + XA_E + N \qquad (1)$$

where

- M is the measured signal,
- X is the response of the transducer and its associated electronics,
- D_F includes the diffraction, attenuation and other factors involved in the propagation of the sound to the flaw and back,
- A_F is the scattering amplitude of the flaw,
- A_M describes the material noise scatterers, including propagation factors,
- A_E describes "echo" noise such as geometrics or ringdown, and
- N is random electronic noise.

This notation differs from that used in Ref. 1 in that Ref. 1's term "p" is the product of our terms "X" and "D" and that we explicitely include a term which describes the "echo noise".

The derivation of an optimum detection algorithm is done in a decision theoretic manner. A detailed description of this derivation is given in Ref. 1. A summary follows: The full problem of distinguishing all flaws larger than a certain size from smaller flaws or no flaw at all generally leads to a mathematically intractable problem. Therefore, a key simplification has been made which leads to detection algorithms which can be implemented in real time

hardware. This assumption is based on the observation that much of the energy scattered from flaws comes from localized areas of the flaw, such as the front surface of a volumetric flaw or the tip diffraction of a crack. As a result, this scattering is impulse-like. We have therefore used a simplified flaw model in which the impulse response of the flaw is modeled as a delta function or a set of a small number of delta functions. This leads to detection algorithms which are of the form of a convolution of the measured signal with a filter function. For the case of modeling the flaw as a single delta function, the filter function is:

$$F(\omega) = \frac{X(\omega)^* \; D(\omega)^*}{C(\omega)} \qquad (2)$$

where $C(\omega)$ is the power spectrum of the noise sources which can't be eliminated by preprocessing and * indicates complex conjugation.

Detection then consists of thresholding the quantity:

$$S(t) = \sum_{\omega} M(\omega) \; F(\omega) \exp(j\omega t) \quad . \qquad (3)$$

This corresponds to a type of matched filter for the detection of impulsive scatterers.

The advantages of the statistcal approach are the following:

1. More accurate detection and characterization of flaws.
2. Automatic adaptation to the particular sample being tested and to the particular instrumentation being used.
3. Statistical algorithms can give confidence measures which can indicate the level of confidence which should be placed in any given estimate which the algorithm makes.

Among the practical implications of the statistical approach are:

1. The ability to detect and size smaller flaws.
2. The ability to detect and size flaws in noisier materials.
3. Increased inspection speed because less highly focussed transducers are needed to detect a given flaw.
4. Less exacting requirements on instrumentation, because the algorithms adapt to the properties of the instrumentation.

The limitations of the statistical approach include:

1. Large flaws can be detected by conventional means. The statistical approach is not needed.
2. Very small flaws will not be detected even by the statistical approach. There is, therefore, a range of flaw sizes for which the technique is appropriate.
3. The statistical approach requires digital processing of the measured data. Currently, this requires more expensive hardware than analog processing, but the margin is narrowing.

III. IMPLEMENTATION ON MEASURED DATA

In order for statistical flaw detection to be of practical use, two things must be proven. First, it must be shown that a significant improvement in flaw detection can be achieved on experimentally measured data, given the limitations of this data. Second, it must be possible to implement the method in algorithms and hardware which operate fast enough to be of use in practical NDE situations.

In this program, we have developed two implementations of statistical flaw detection. The first is a "research algorithm" which is written in the ISP signal processing language and provides a flexible vehicle for examining the performance of a variety of forms of detection algorithms, statistical and conventional. The second is a real time algorithm which is implemented in the Digital Ultrasonic Instrument (DUI).

A. Research algorithm

The first form in which the statistical approach to flaw detection has been implemented is a general purpose algorithm, written in ISP, by means of which a number of variations of the algorithm were tested and evaluated. The algorithm consists of a setup or training phase, followed by a testing phase.

1. The setup phase consists of the following parts:
   a. Estimate electrical and A/D converter noise from a set of waveforms collected at a single location on the sample. The algorithm calculates the mean waveform and the variance waveform of this set. The variance waveform is used to estimate of the power spectrum of the electrical and A/D converter noise and can be used to select the amount of signal averaging to be used in subsequent measurements so as to reduce the amount of these noises to a desired level.
   b. Estimate echo noise and material noise from a set of waveforms collected at a variety of nominally identical flaw free locations in the specimen. The algorithm again calculates the mean and variance waveforms. The mean waveform is an estimate of the echo noise (noise which is independent of position). It is saved and subtracted from each new data waveform that is acquired. The variance waveform is used to estimate of the power spectrum of the remaining noises and is used for $C(\omega)$ in the detection filter.
   c. The system response $X(\omega)$ is measured by means of the reflection of the sound beam from a flat surface in the far field of an unfocussed transducer or at the focus of a focussed transducer.
   d. The diffraction $D(\omega)$ which the sound beam undergoes in reaching the flaw location is calculated using formulae developed by Thompson, et.al.[9]

Note that if the flaw is sufficiently in the far field of the transducer at all frequencies of interest, then $D(\omega)$ is the same for flaw and system response measurements and can be ignored. To the extent that the flaw is not in the far field, the diffraction can be determined theoretically, as described in the previous paragraph, or experimentally, by means of a scatterer of known properties at the exact distance of the flaw. Both of these approaches are limited because, in practice, it is difficult either to know the sound field well enough to reproduce near field effects theoretically, or to have a scatterer whose properties and position are known accurately enough to reproduce them theoretically.

e. The detection filter $F(\omega)$ (Eq. 2) is now calculated from the quantities determined above.
f. A detection threshold must be set. This can be done either theoretically using the measurement model or experimentally using reference specimens as is currently done in most NDE measurements. Neither approach is entirely satisfactory because in neither case can one be sure that the conditions in the test piece have been accurately duplicated. Because the purpose of our measurements was to study the algorithms rather than to detect specific flaws, a threshold was not selected, but rather the detection function itself was displayed for analysis.

2. The test phase consists of the following parts:
   a. A candidate waveform is acquired.
   b. The echo noise is subtracted from it.
   c. Two detection algorithms are then applied to the data: video detection and statistical detection. Video detection is performed by rectification followed by low pass filtering using a frequency domain Hanning window centered at zero frequency and with halfwidth equal to twice the transducer center frequency. The statistical detection is performed by filtering the signal using the filter $F(\omega)$ defined above.
   d. A display is provided of the waveforms at various steps in the computation process and of the waveforms output by each algorithm.

B. Real-time algorithm

In order for a detection technique to be of practical use, it must be able to be implemented in a form which will operate at the speed at which conventional ultrasonic inspections are performed. In order to demonstrate this capability and in order to provide for more rapid testing of the statistical approach, a real-time version of these algorithms has been implemented. This part of the work was funded by the CANDIS program.[10] The algorithms were implemented on the Digital Ultrasonic Instrument (DUI),[11] which is a high speed all-digital instrument for performing sophisticated calcula-

tions on ultrasonic signals. The DUI controls the motion of the Ultrasonic Test Bed[12] in order to scan over the specimens under test. The detection algorithms implemented on the DUI are simpler than the research algorithm described above and therefore serve as a test of what simplifications can be made in the original algorithm in order to speed the computations without significantly reducing the quality of the results. The real-time algorithm also consists of a set-up or training phase, and by a testing phase.

1. In the set-up phase, the DUI guides the operator through the series of measurements required to design the detection filter:
   a. The DUI first asks the operator to provide an echo from a flat surface in order to determine the system response. The DUI provides an oscilloscope display of the waveform to guide him in his adjustments of the instrument. When the operator signals that he has the correct signal, the DUI acquires it, calculates its frequency spectrum and inserts it into the detection filter. No attempt is made to correct for diffraction in this algorithm, as it is assumed that the flaw is sufficiently in the far field of an unfocussed transducer or sufficiently close to the focus of a focussed transducer that such a correction is not needed.
   b. The DUI then asks the operator for a region of the sample over which to make a coarsely spaced scan in order to determine the noise present in the sample. It is desirable that there be few or no flaws in this region. The DUI scans the region, calculates the variance of the noise waveforms and thus determines $C(\omega)$. In this algorithm the echo noise was not estimated and saved for the purpose of later subtraction, although this capability has been demonstrated in the DUI before.
   c. The DUI then calculates the detection filter.
   d. Because the algorithm also calculates the video detection waveform, it is necessary to calculate the required lowpass filter. In order to do this, the DUI asks the operator the center frequency of the transducer, although it could as well have measured this from the system response spectrum.

2. In the testing phase, the DUI performs the following steps:
   a. The Testbed is scanned to the next position to be measured.
   b. The waveform is acquired, with optional signal averaging.
   c. Three detection algorithms are applied to the waveform:
      Peak of the sampled rf waveform
      Peak of the video waveform
      Peak of the statistical waveform
      The three peak values are stored for each point inspected. The sampled rf waveform is included in the set because it would be the easiest to implement in a digital system.
   d. At the end of the scan, three graphs are plotted. Each is the peak output of one of the detection algorithms.

IV. RESULTS

This section presents two sets of results. First are the results of applying the research version of the statistical detection algorithm to a set of data in which the level of electrical and A/D converter noise have been varied by changing the amount of signal averaging used in acquiring the data. Second, we present the results of using the real time algorithm while scanning a specimen.

The specimen used in these measurements is a block of plastic[13] in which crack-like flaws have been induced by laser damage (Figure 1). The sample has a cylindrically cut surface which simulates the borehole of turbine engine components. The flaw on which these measurements is based is a crack 0.5 mm in diameter. Optical inspection shows it to be very flat and very nearly circular. The normal to the crack is inclined at an angle of 60° with respect to the normal to the cylindrical surface.

A. Results of the research version of the algorithm

The flaw is fairly easy to detect using a properly selected focussed transducer. In order to provide a greater challenge for the detection algorithm, the measurements were performed in a less than optimum manner. First, an unfocussed transducer was used, giving a smaller S/N than a focussed one would have. Recall that one of the benefits which is expected from the use of the statistical approach is that faster scanning will be possible by the use of less highly focussed transducers. Second, the transducer diameter was large (0.5 in), further decreasing the flaw signal relative to the noise. Third, the flaw was located at the first near-field null of the transducer at approximately the transducer's center frequency (5 MHz). The result is that the flaw signal is only approximately 1 LSB in amplitude at the input to the A/D converter.

Figure 2 shows a set of 6 waveforms acquired with varying amounts of signal averaging while the transducer was aimed at the flaw. Each is labled with a relative signal-to-noise ratio based on the amount of signal averaging used. The flaw is visible at 34 μs in the higher S/N cases. At the beginning of the waveform is some "echo" noise due to the ringdown of the front surface echo. In the lower S/N cases, the quantization noise of the A/D converter is clearly visible.

The analysis of the noise processes gave the following results: Figure 3 shows the mean and the power spectrum of the variance of a set of waveforms collected with the transducer at a fixed position. The mean contains echo noise, material noise and the flaw. The noise power spectrum is a measure of the electrical and A/D converter noise. The sharp structure at 12.5 Mhz is due to clock noise in the A/D converter (Biomation 8100). Figure 4 shows the mean and

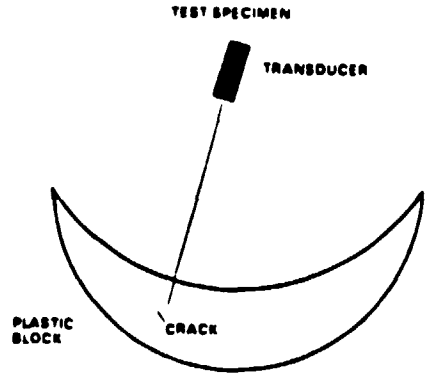

Fig. 1. Plastic test specimen with laser induced crack.

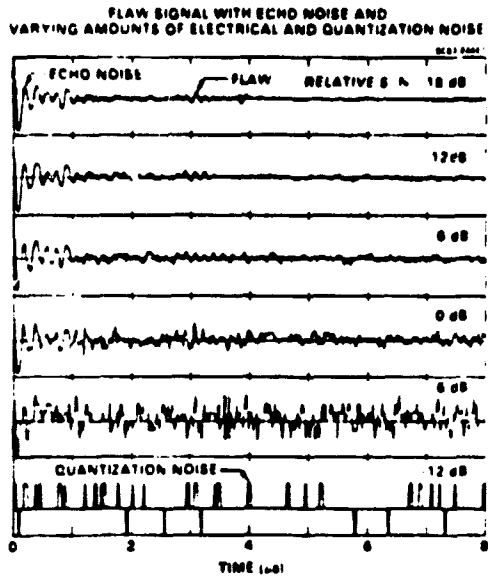

Fig. 2. Set of flaw signals with varying amounts of noise provided by varying the amount of signal averaging.

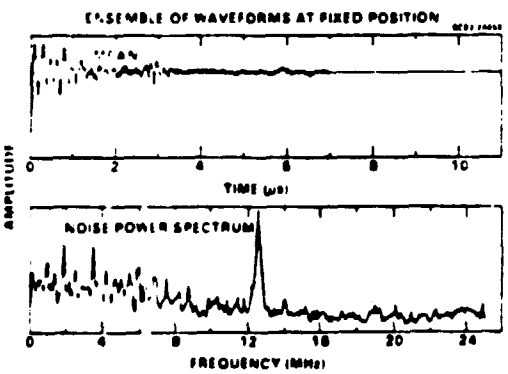

Fig. 3. Mean and noise power spectrum of a set of waveforms collected at a fixed position.

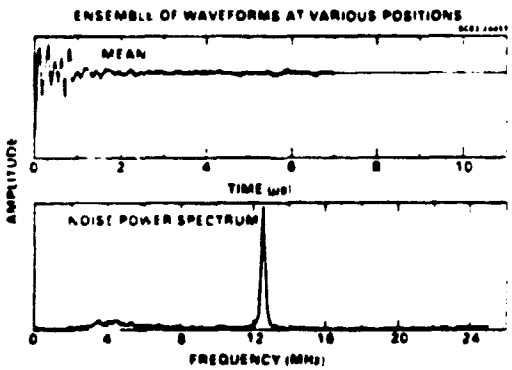

Fig. 4. Mean and noise power spectrum of a set of waveforms collected at various flaw free positions.

the power spectrum of the variance of a set of waveforms collected as the transducer was moved to a variety of flaw free locations. The mean in this case is the echo noise which can be removed from measured data by subtraction. The variance contains all of the random noises present in the signal, including material, electrical and A/D converter. It is this waveform that is used as the basis for the noise power spectrum $C(\omega)$ in the detection filter.

Figure 5 shows the steps involved in determining the system response function. The first two curves are the reference waveform obtained from a flat surface echo and its spectrum. The third curve is the calculated diffraction D for the flaw location. Note the near field null at 5 MHz. The fourth curve is the product XD.

Figure 6 contains the remainder of the steps involved in preparing the detection filter. The first curve is the measured noise spectrum (from figure 4). Because it is an estimate based on a small number of samples, it not as smooth as the expectation of the noise process itself. We have therefore smoothed it by means of a low pass filter applied to the spectrum (second curve). Finally, the filter function F is calculated (third curve). Note that the A/D clock noise will be completely eliminated from the measured data because the transducer has no energy at 12.5 MHz and therefore the filter ignores this frequency.

Figure 7 shows the results of applying the algorithm to the waveform labeled "6dB". The upper curve is the measured waveform. The middle curve is the result of applying video (envelope) detection and the lower curve is the result of the statistical detection algorithm. Video detection does not clearly distinguish the flaw, but a significant response due to the front surface ringdown is seen. The statistical approach, on the other hand, shows the flaw clearly standing out above all the other noises.

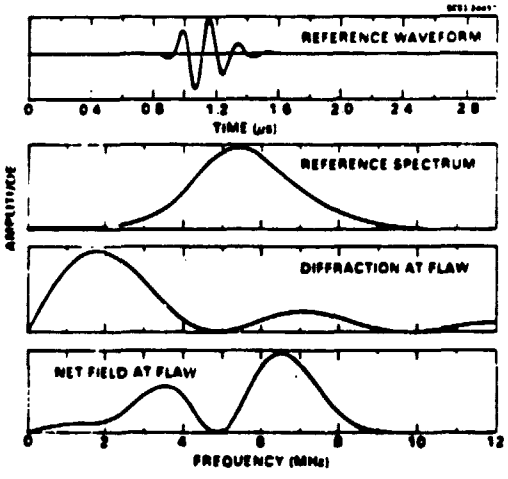

Fig. 5. Signals used in calibration of detection algorithm: a) system response from flat surface echo, b) spectrum |X| of a), c) calculated diffraction |D| at flaw location, d) |XD|.

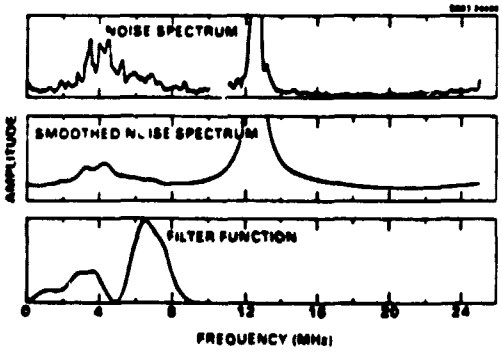

Fig. 6. Additional calibration signals: a) Estimated noise spectrum C(ω), b) smoothed noise spectrum, c) filter function |(XD)*/C|.

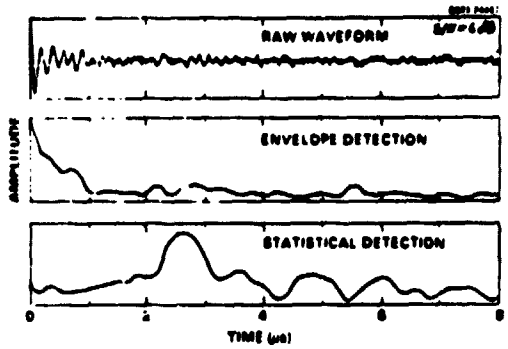

Fig. 7. Comparison of envelope (video) detection and statistical detection for S/N = 6 dB.

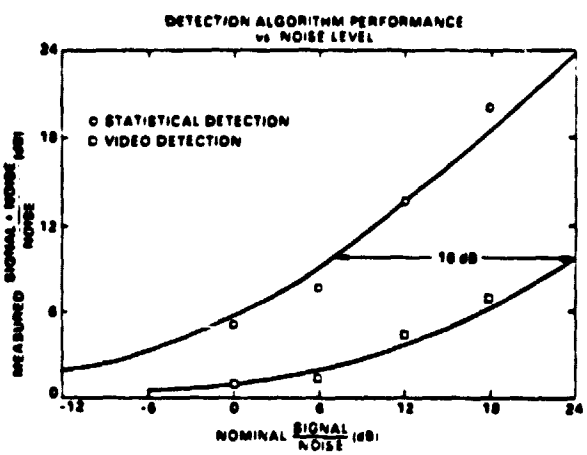

Fig. 8. Performance of statistical and video detection algorithms vs noise level. Solid curves are theoretical fits to data. Statistical algorithm has 16 dB inherent advantage.

The results of applying the two algorithms to the six data waveforms are summarized in Fig. 8. The horizontal axis is the nominal signal-to-noise of the waveform. The vertical axis is the measured performance of the algorithm, expressed as the peak height of the detected signal at the time when the flaw is known to be present, divided by the peak height of the detected signal at any other time during the measurement. (In computing this measure, the detected signal due to front surface ringdown has been ignored, since this is not present in many measurement situations.) The circles show the results for the statistical detection algorithm. For the two lowest S/N cases, the flaw was not detected. The squares show the results for the video detection algorithm. It is likely that this algorithm did not detect the flaw in any of the four lowest S/N cases. The solid curves are a theoretical calculation of the expected (S+N)/N for various values of S/N. Each curve was fit to the corresponding set of results by varying S (i.e. sliding the curve horizontally). The curves for the two algorithms are separated by 16 dB, indicating that the inherent ability of the statistical algorithm to separate signals from noise is about 16 dB better than for video detection in this case.

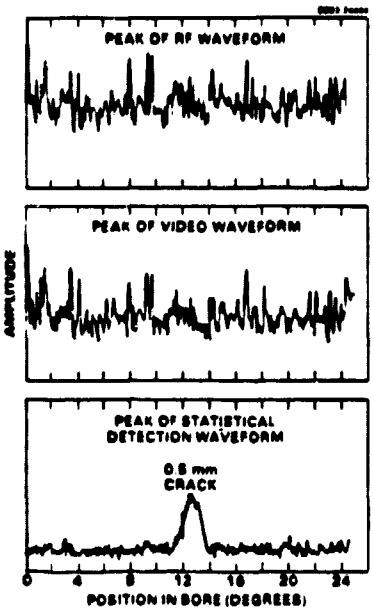

Fig. 9 Results of angular scan over crack using real time algorithm. Statistical algorithm successfully detects crack.

B. Results of the Real-Time Algorithm

The real time algorithm was used in conjunction with the Ultrasonic Testbed to scan a transducer over the specimen containing the flaw described above. The pivot point of the transducer manipulator was positioned at the center of curvature of the cylindrical surface of the sample and the transducer was then scanned over a 25° angular range which included the flaw. Figure 9 shows the peak amplitude of the signals produced by each of the three detection algorithms as a function of position. Neither the raw digitized r.f. waveform nor the video waveform detected the presence of the crack. The statistical algorithm, on the other hand, did detect it, with a signal-to-noise of about 12 dB.

V. CONCLUSIONS

The method presented here makes use of an explicit knowledge of the noise processes in order to design a flaw detection algorithm which optimally detects flaws in the presence of such noise. A key assumption which makes the approach implementable in a simple form is to model the flaw as having an impulse response function which consists of a set of delta functions.

Experimental results using this statistical approach show a significant improvement in the detectability of a crack-like flaw relative to the results obtained with conventional video detection. This approach promises to provide a number of advantages in practical testing situations, including detection of smaller flaws, faster scanning due to the use of less highly focussed transducers, and less need for operator optimization of the measurement process.

REFERENCES:

1. K.W. Fertig, J.M. Richardson, R.K. Elsley, Flaw Detection: Theory", This proceedings.
2. K. A. Marsh, J. M. Richardson, R. C. Addison, R. K. Elsley, "The Automation of the Born Inversion for Ultrasonic Flaw Sizing", in Rev. of Prog. in Quant. Nondestruc. Eval. 2, D. O. Thompson, D. E. Chimenti, Eds. (Plenum, New York, 1983), pp. 975-987.
3. J.M.Richardson, R.K.Elsley, "Extraction of Low Frequency Properties From Scattering Measurements", 1979 Ultra. Sym. Proc. IEEE, 79CH1482-9, pp.336-341, (1979)
4. Dick Elsley, John Richardson, Bob Addison, "Optimum Measurement of Broadband Ultrasonic Data", 1980 Ultra. Sym. Proc. IEEE, 80CH1602-2, pp.916-921, (1980)
5. J. M. Richardson, R. K. Elsley, "Semi-adaptive Approach to the Extraction of Low-frequency Properties from Scattering Measurements", 1980 Ultra. Sym. Proc., IEEE, pp.847-851, (1980)
6. L.A.Ahlberg, R.K.Elsley, L.J.Graham, J.M.Richardson, "Long Wavelength Ultrasonic Characterization of Inclusions in Silicon Nitride", Proc. of the DARPA/AFML Rev. of Prog. in Quant. NDE, AFWAL-TR-80-4078, pp.656-662, (1980).
7. R.K.Elsley, L.A.Ahlberg, J.M.Richardson, "Low Frequency Characterization of Flaws in Ceramics", Proc. of the DARPA/AFML Rev. of Prog. in Quant. NDE, AFWAL-TR-81-4080, pp.151-164, (1981).
8. R.K.Elsley, "Inversion Algorithms for Crack-like Flaws", in Rev. of Prog. in Quant. Nondestruc. Eval., D.O. Thompson, D.E. Chimenti, eds., Plenum, New York, pp.537-545, (1982)
9. R. B. Thompson, T. A. Gray, "Analytic Diffraction Corrections to Ultrasonic Scatterubg Measurements", in Rev. of Prog. in Quant. Nondestruc. Eval., 2, D. O. Thompson, D. E. Chimenti, Eds. (Plenum, New York, 1983), pp. 567-586.
10. CANDIS is an acronym for Computer Aided Non-Destructive Inspection System. CANDIS is a Technology Modernization Program within the B1-B Contract F33657-81-C-0210.
11. R.K. Elsley, "The Digital Ultrasonic Instrument", in Rev. of Prog. in Quant. Nondestruc. Eval., 2, D.O. Thompson, D.E. Chimenti, Eds. (Plenum, New York, 1983), pp. 1487-1500.
12. The Ultrasonic Testbed is an automated immersion testing system developed under Air Force Contract F33615-78-C-5164.
13. This sample was provided by Dave Hsu of Colorado State Univ.

DISCUSSION:

From the Floor: You mentioned getting rid of the echo noise by subtraction. If there's any motion in the transducer, that turns into a differentiation that can be a very noisy process. Do you anticipate any problems with that?

R.K. Elsley: The question was about the practical aspect of implementing subtraction. Of course, you can do the subtraction

either in the time or frequency domain because it is a linear process.

Now about jiggles in the transducer which produce the effect that the signal doesn't arrive at quite the same time when you do subtraction. That certainly does happen. One of the techniques that we have used in some of this processing is to specifically time align the signal before doing the subtraction. Again, it requires a little extra computation capability, but by doing time aligning, we can use subtraction in a variety of areas such as in this kind of processing and phased array imaging. We can often get 25 DB of suppression of unwanted signals by careful subtraction.

P.M. Gammell (Sigma Research): I notice you are looking for signals which are below the least significant data recorded. Am I correct that this process actually requires the existence of noise and requires that the noise have certain statistics?

R. K. Elsley: Yes, I would agree. That's not my choice for doing such measurements, of course. It was just a trick to use to get added signal-to-noise for testing the algorithm, but I agree with your statement.

J.A. Simmons (National Bureau of Standards): Can you use this method to improve on time resolution or positioning resolution for the flaw?

R. K. Elsley: Yes. For example, one of the items that is needed to do the Born inversion is a very accurate measure of the location of the center of the flaw. The correct way to do that is by using the low frequency data. We have a statistically based approach for making an optimal estimate of where the center of the flaw is based on low frequency data. That's one that is specifically addressed by this technique.